Lab on a Chip

ROYAL SOCIETY OF CHEMISTRY

PAPER

View Article Online
View Journal

Check for updates

Cite this: DOI: 10.1039/d5lc00549c

Investigation of fluid diffusion kinetics in nanochannels using micro-Raman spectrometry

Jingyu Chen,[a] Haowei Lu,[a] Kecheng Zeng,[ab] Haidong Ji,[a]
Peixue Jiang[a] and Ruina Xu*[a]

Received 4th June 2025,
Accepted 11th August 2025

DOI: 10.1039/d5lc00549c

rsc.li/loc

Fluid diffusion kinetics in nanopores is crucial for energy conversion and utilization but influenced by complex pore structure and fluid–wall interactions. Traditional experiments are difficult to decouple diffusion in nanopores and micron-pores, molecular simulations are time-consuming when handling pores with diameters larger than 10 nm, and nanofluidic experiments *via* conventional optical methods face challenges in measuring fluid concentrations. Here, we report a novel Concentration Decay Method combining nanofluidics and microscopic Raman spectroscopy to investigate diffusion in nanochannels. A "channel-channel-cell" chip design enables real-time detection of fluid concentrations in microcells and measurement of diffusion coefficients in nanochannels, and a self-made temperature control module enables precise adjustment of fluid temperature. By this method, interdiffusion experiments of an *n*-octane–1-octene mixture and *n*-octane–cyclooctane mixture in nanochannels (depths = 21–173 nm) are conducted to explore oil diffusion in shale. We report that the oil diffusion in nanochannels still conforms to Fick's diffusion law, and the diffusion coefficients in channels with a minimum depth of 21 nm and at different temperatures (295–383 K) exhibit no obvious deviation from the bulk phase, suggesting that fluid–wall interactions have no significant effect on diffusion kinetics in our experiments. The consistency of the experimental results and classical predictions also validates the reliability of our Concentration Decay Method, which fills the gap in research on fluid diffusion in nanopores and has promising application prospects. Diffusion in nanochannels with more types of fluids, more complex channel structures and smaller depth of the channel can be furthered investigated by this method.

1. Introduction

Shale oil is a type of globally abundant unconventional oil resource that has received significant attention in recent years, demanding a thorough understanding of fluid transport in shale reservoirs.[1–3] Specifically, diffusion processes driven by fluid concentration gradients are prevalent during primary oil migration in kerogen,[4] *in situ* conversion of organic matter,[5] and gas injection for enhanced oil recovery.[6,7] Compared to conventional oil reservoirs, shale reservoirs typically have nanopores with diameters less than 100 nm.[8–10] The diffusion kinetics in nanopores is more complicated than that at the macroscopic scale due to strong fluid–wall molecular interactions and a large surface-to-volume ratio.[11]

Previous studies on fluid diffusion in nanoporous materials with average pore diameters ranging from 0.1 to 10 nm have reported abnormal diffusion kinetics compared to Fick's law, which is highly sensitive to the pore structures and fluid types.[12,13] For example, Zeng *et al.* found the restricted diffusion kinetics of CO_2 and methane in organic nanopores due to nanoconfinement and competitive adsorption; in contrast, Yuan *et al.* reported hyperloop-like diffusion of long-chain alkanes in zeolites with faster kinetics due to linear orientation of alkane molecules.[14,15] For diffusion in shale nanopores, the pore size ranges from sub-nm to sub-100 nm, and the pore shape and connectivity vary spatially; besides, shale oil is a mixture of multi-component hydrocarbons with various molecular structures. Hence, the more complex pore structures and fluid types make diffusion in shale nanopores more complex.

Traditional core-scale experiments have been conducted to reveal macroscopic diffusion behaviors in shale porous media. Yuan *et al.* investigated methane diffusion and adsorption behaviors in shale cores with a bimodal pore size distribution and found that the diffusion kinetics can be

---

[a] Key Laboratory for Thermal Science and Power Engineering of Ministry of Education, Department of Energy and Power Engineering, Tsinghua University, Beijing 100084, People's Republic of China. E-mail: ruinaxu@mail.tsinghua.edu.cn
[b] Shanxi Research Institute for Clean Energy, Tsinghua University, Taiyuan 030032, People's Republic of China

described by a bidisperse model related to the pore size distribution.[16] Wanyan *et al.* conducted an experiment on propene diffusing into initially oil-saturated shale cores with different permeability and reported a positive correlation between the apparent diffusion coefficient and the core permeability, which was speculated due to more tortuous diffusion paths.[17] However, core-scale experiments investigate the averaged fluid diffusion behaviors by treating the complex shale porous media as a whole, so it is difficult to decouple the diffusion kinetics in nanopores and micron-pores and analyze its influencing factors including pore structure and fluid–wall interactions.

Molecular-scale simulations are an alternative method to unveil the essence of fluid diffusion in shale nanopores. Simulations of chain-like alkane transport in smooth nanoslits or nanopores have shown that near-wall alkane molecules strongly affected by fluid–wall interactions tend to align parallelly in layers.[18–21] The unique characteristics of near-wall fluid molecules lead to deviated local self-diffusion coefficients, especially in the direction normal to the pore wall.[22,23] However, limited by computing power, the pore sizes in these simulations generally do not exceed 10 nm. For pores with diameters ranging from 10 to 100 nm, there is currently no reliable method to investigate fluid diffusion kinetics within.

Thanks to the advancements in lithography, etching, and bonding technologies, it is now feasible to investigate fluid transport in nanopores by visualized experiments on nanofluidic chips with feature sizes reaching down to 10 nm scale. Recently, progress on flow kinetics and phase behaviors in shale reservoirs has been made based on nanofluidic experiments.[24–29] Nanofluidic chips can be further combined with temperature control modules to achieve precise control of fluid temperature.[30] However, nanofluidic studies on fluid diffusion are limited due to the difficulty of measuring the concentration of diffusing solute. Balducci *et al.* conducted an experiment on double-stranded DNA confined diffusion in nanochannels; Yang *et al.* studied single-file diffusion of protein molecules in a nanopore array; Zhong *et al.* reported slower diffusion kinetics of Rhodamine B nanoparticles in an 8 nm-deep nanochannel than predicted.[31–33] These mentioned studies quantitively measured the concentration of diffusing solutes by their fluorescence intensity; however, the majority of fluids in shale reservoirs are transparent and lack fluorescence signals, making it difficult to measure their concentration by conventional optical methods.

Raman spectroscopy is a reliable technique for non-destructively obtaining compositional information of substances, and can be employed to analyze real-time variation of micro-scale substance composition when combined with a microscope.[34,35] Based on characteristic Raman peaks, fluid types with different functional groups or chemical bonds can be easily distinguished. Furthermore, quantitative measurement of fluid concentration can be achieved by normalizing Raman peak intensities or areas,[36–38] enabling investigation on diffusion kinetics in microfluidic or nanofluidic chips. To date, studies using Raman spectroscopy for diffusion in microchannels have been reported,[38–40] but no nanofluidic experiment on diffusion in nanochannels has been reported yet. Raman spectroscopy necessitates a trade-off between small sampling intervals and high signal-to-noise ratios, while the Raman signal of fluid in nanochannels is typically too weak for real-time concentration measurement. Therefore, nanofluidic studies on diffusion in nanochannels still require a design of experimental system and methods.

In this work, we report a novel Concentration Decay Method combining nanofluidics and microscopic Raman (micro-Raman) spectroscopy to investigate fluid diffusion in nanochannels. A “channel-channel-cell” structure in nanofluidic chips is specifically designed for detecting diffusion kinetics in nanochannels, and a temperature control module is made for adjustment of fluid temperature. Experiments on hydrocarbon interdiffusion in nanochannels (depths = 21–173 nm) at different temperatures (295–383 K) are conducted. *N*-Octane, 1-octene and cyclooctane are selected as interdiffusion fluids. Diffusion coefficients in nanochannels are obtained and discussed.

2. Materials and method

2.1 Design and fabrication of nanofluidic chips

Each nanofluidic chip consists of 9 nanochannels (depths = 21, 37, 52, 85, 115, 173 nm, width = 5 μm, lengths = 100, 300, 1000 μm), 9 microcells (cube-shape, side length = 10 μm), 1 microchannel (depth = 10 μm), 2 reservoirs and 1 thermocouple channel (depth = width = 150 μm), as shown in Fig. 1a and b. One end of the nanochannels is perpendicularly connected to the microchannel and the other to the microcells, and the “channel-channel-cell” structure is formed. The ends of the microchannel are connected to the reservoirs. The reservoirs are connected to the external pipelines. The end of the thermocouple channel is only 100 μm away from the microcells.

The schematic of the interdiffusion process in a nanochannel is illustrated in Fig. 1c. There is a concentration gradient between the microchannel and microcell leading to interdiffusion. The real-time variation of fluid concentrations in the microcells during interdiffusion is characterized by Raman spectroscopy, and thus the diffusion kinetics in nanochannels can be indirectly detected.

The nanofluidic chip features a silicon–glass dual-layer structure. The fabrication procedures, as illustrated in Fig. 1d, are similar to those reported in the literature,[27,41,42] including photolithography, dry etching, surface thermal oxidation, and anodic bonding. First, the patterns of nanochannels and microchannels are defined on the photoresist through photolithography. Subsequently, these patterns are etched onto a single-crystal silicon wafer (thickness = 500 μm) using reactive ion etching (RIE). The photolithography and etching processes for nanochannels

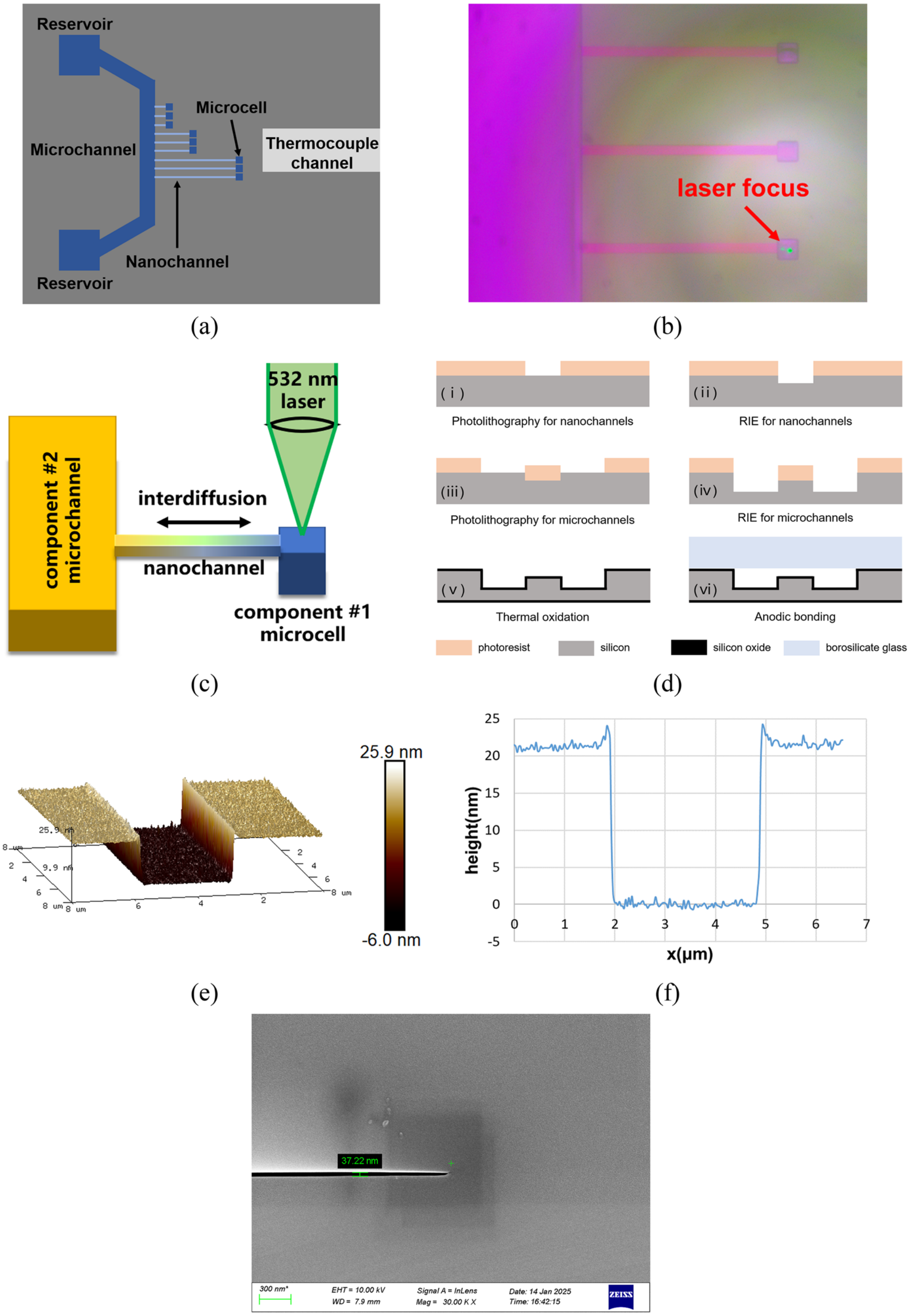

(a) (b) (c) (d) (e) (f) (g)

Fig. 1 Design and fabrication of nanofluidic chips. (a) Top-view diagram of nanofluidic chips showing the "channel-channel-cell" structure. (b) Optical microscopy image of the experimental section. (c) Schematic depicting the interdiffusion process in a nanochannel. (d) Fabrication procedures of nanofluidic chips. (e) and (f) Three-dimensional surface morphology and a cross-sectional profile of a 21 nm deep nanochannel obtained by AFM; (g) SEM image revealing the cross-section structure of a 37 nm deep nanochannel on a bonded chip.

and microchannels are performed separately. Following this, a thermal oxidation step is conducted to grow a silicon oxide layer (thickness = 300 nm) on the silicon surface. A borosilicate glass substrate (thickness = 500 μm, BOROFLOAT® 33) serves as the chip cover. Prior to bonding, the silicon wafer and glass substrate are cleaned with piranha solution (a 3 : 1 mixture of 98% H_2SO_4 and H_2O_2). The surface morphology of the etched nanochannels is characterized using atomic force microscopy (AFM), revealing a root mean square roughness (Ra) of approximately 0.7 nm at the channel bottom, as shown in Fig. 1e and f. Finally, the silicon wafer and glass substrate are bonded together using a

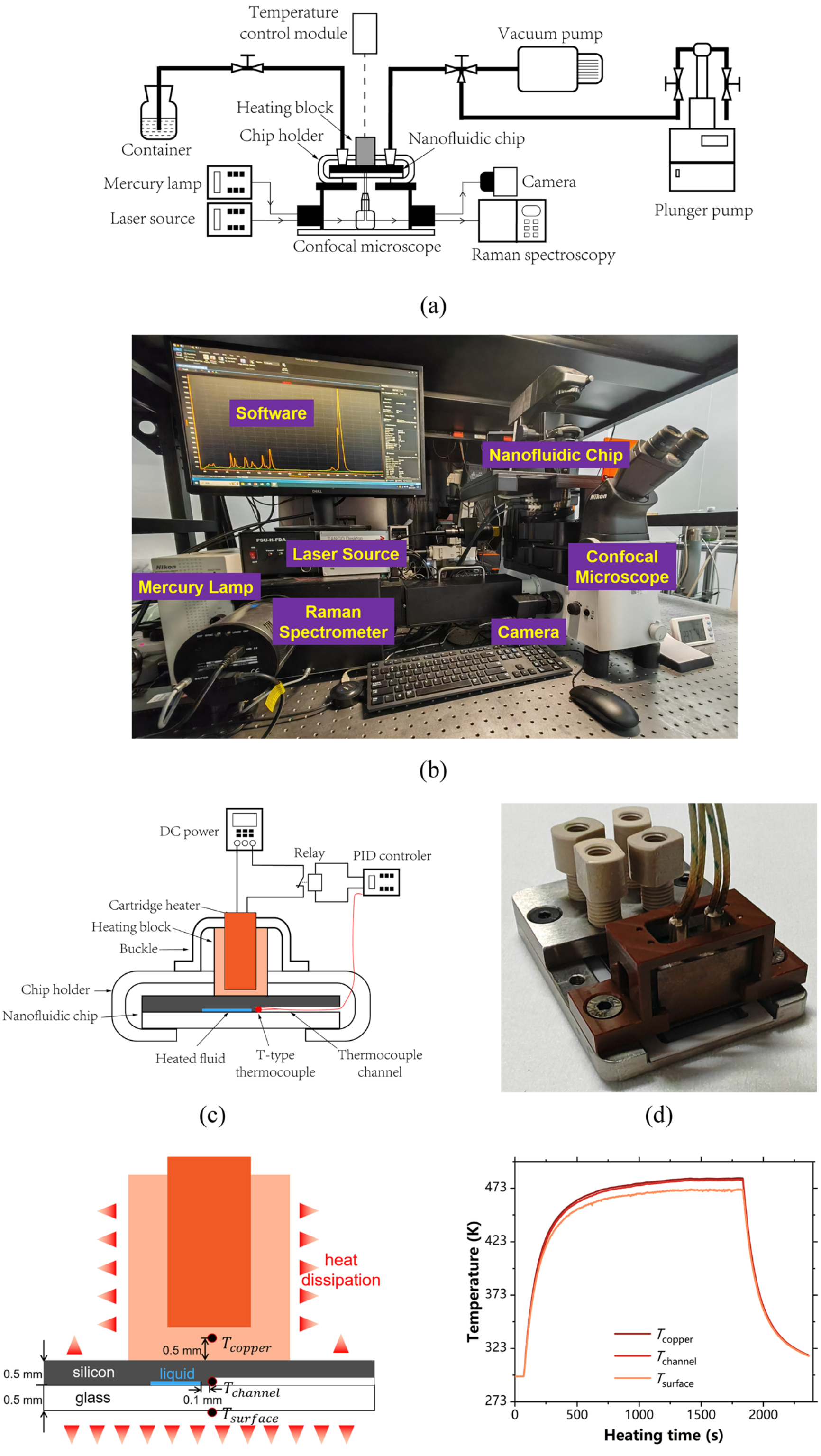

(a)

(b)

(c) (d)

(e) (f)

Fig. 2 Micro-Raman experimental system. (a) and (b) Schematic illustration and photograph of the experimental system. (c) and (d) Schematic illustration and photograph of the temperature control module. (e) Setting of three temperature measurement points. (f) A heating test showing the difference among T_{copper}, T_{channel} and T_{surface}.

custom-developed anodic bonding platform. The cross-sectional view of a bonded nanochannel, observed *via* scanning electron microscopy (SEM), is presented in Fig. 1g, confirming that the upper and lower surfaces are aligned reasonably parallel.

2.2 Experimental system

The experiments are conducted on a micro-Raman experimental system, which consists of nanofluidic chips, a chip holder, a confocal microscope, a camera, a Raman

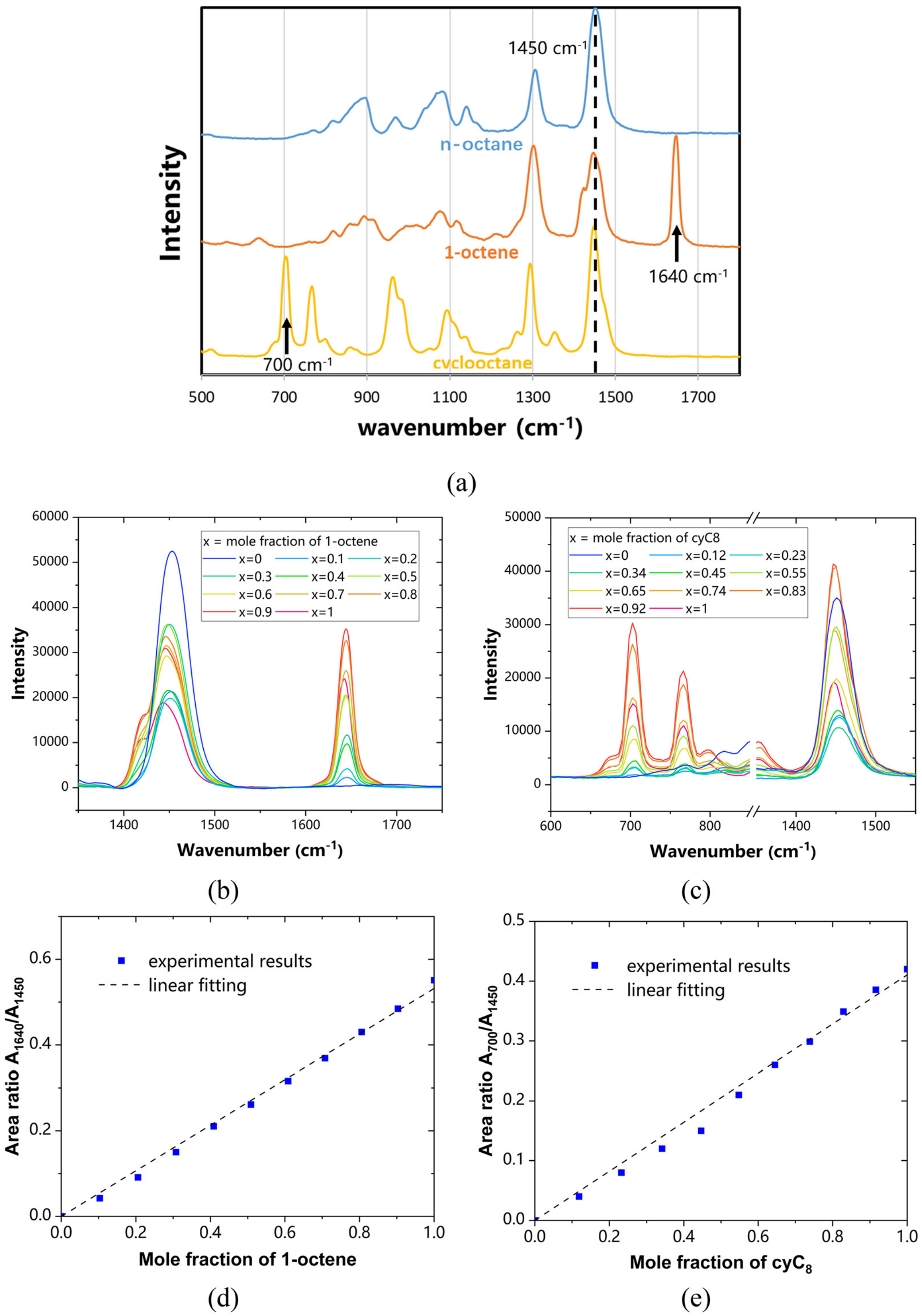

Fig. 3 Calibration between Raman spectral signals and fluid concentrations. (a) Raman spectra of pure *n*-octane, 1-octene and cyclooctane. (b) and (c) Raman spectra of binary mixtures of *n*-octane and 1-octene with different $x_{1\text{octene}}$, and of binary mixtures of *n*-octane and cyclooctane with different x_{cyC8}. (d) and (e) The linear relationship between A_{1640}/A_{1450} and $x_{1\text{octene}}$, and between A_{700}/A_{1450} and x_{cyC8}.

spectrometer, a mercury lamp, a laser light source, auxiliary pumps, and a temperature control module, as depicted in Fig. 2a and b. The nanofluidic chips are fixed in a self-made holder, which is then fixed on the specimen stage of the confocal microscope (Nikon Ti2-U). The mercury lamp and camera are used to locate and focus on the position where Raman spectra need to be collected. The laser light source with a wavelength of 532 nm and a power of 100 mW is used for Raman spectra excitation. The Raman spectrometer (HRS-300S) collects spectra at the position of the microcells on chips during the interdiffusion process with a wavenumber resolution of 0.2 cm^{-1} and a spatial resolution of 1 μm. The auxiliary pumps, including a vacuum pump and a plunger pump, are used to establish the initial fluid distribution in the chips prior to the beginning of interdiffusion.

The self-made temperature control module can be installed on the chip holder, as depicted in Fig. 2c and d. The working principle of the module is to use a copper heating block embedded with cartridge heaters and closely adhering to the experimental section of the nanofluidic chip to heat the interdiffusion fluid. T-type thermocouples with a diameter of 100 μm inserted into the thermocouple channel on the chip are used to monitor the real-time fluid temperature. A PID controller is used to control the switch of the heating circuit to adjust temperature. To reduce the contact thermal resistance between the cartridge heater and the heating block, between the heating block and the chip, and between the thermocouple and the thermocouple channel, the gaps between the above-mentioned solid surfaces are all filled with high-temperature resistant thermal grease.

To demonstrate that the thermocouple inside the chip can reflect the fluid temperature, three thermocouples are respectively fixed in a hole 0.5 mm away from the bottom of the copper block, in the thermocouple channel and on the glass surface, and the three measurement points are vertically aligned, as shown in Fig. 2e. When the system is heated to about 473 K for test, it is found that $T_{\mathrm{copper}} - T_{\mathrm{channel}} \approx 1.5$ K and $T_{\mathrm{channel}} - T_{\mathrm{surface}} \approx 9.4$ K, as shown in Fig. 2f. The reasons for the temperature difference among the three measurement points include the thermal resistance of copper, silicon and glass, the contact thermal resistance between copper and silicon, and the convective heat transfer between the surface of the chip and the air. Relatively, the thermal resistance between the end of the thermocouple channel and nanochannels can be neglected, thus T_{channel} can best represent the temperature of fluid in nanochannels.

2.3 Fluid properties

N-Octane, 1-octene and cyclooctane, three representative components of shale oil, are selected as interdiffusion fluids due to their distinctly different Raman peaks. As shown in Fig. 3a, all of three fluids exhibit a Raman peak at about 1450 cm^{-1} corresponding to the bending vibration of CH_2 and CH_3 groups, while only 1-octene exhibits a Raman peak at about 1640 cm^{-1} corresponding to the stretching vibration of C═C double bonds, and only cyclooctane exhibits a Raman peak at about 700 cm^{-1} related to vibrations of the ring chain.[43,44] Fig. 3a also shows the Raman spectrum of a vacant microcell, indicating that the background signal from the nanofluidic chips does not interfere with 700, 1450, and 1640 cm^{-1} Raman peaks. The self-diffusion coefficients of bulk-phase *n*-octane, 1-octene and cyclooctane at atmospheric pressure and 295 K are about 2.2×10^{-9}, 2.2×10^{-9} and 0.52×10^{-9} $m^2\ s^{-1}$, respectively, as reported in the literature.[45] The boiling points of the three fluids at atmospheric pressure are 399, 395 and 424 K, respectively.

2.4 Quantitative measurement of fluid concentration

Calibration between Raman spectral signals and fluid concentrations is conducted. Although the intensity and area of Raman peaks are concentration-dependent, it is inappropriate to directly use their absolute values to characterize fluid concentrations because of fluctuations of laser power, focusing position, exposure time and environmental noise during sampling. Fig. 3b shows the Raman spectra of binary mixtures of *n*-octane and 1-octene with different mole fractions in the bulk phase. The 1640 cm^{-1} peaks can be regarded as the "fingerprint" of 1-octene. However, due to the variation in the focusing position for each Raman spectrum sampling, the intensity and area of both 1450 and 1640 cm^{-1} peaks do not follow a strictly linear relationship with the mole fraction of 1-octene. Normalizing peak intensity and area can effectively reduce the errors introduced by these factors.[36] In this study, we use the area ratio of the 1640 cm^{-1} and 1450 cm^{-1} peaks, A_{1640}/A_{1450}, to characterize the concentrations of *n*-octane and 1-octene. As shown in Fig. 3d, A_{1640}/A_{1450} increases with increasing mole fraction of 1-octene, and they exhibit a highly linear correlation.

Similarly, the 700 cm^{-1} peaks can be regarded as the "fingerprint" of cyclooctane, and A_{700}/A_{1450} is used to characterized the concentrations of *n*-octane and cyclooctane, which also correlates linearly with the mole fraction of cyclooctane, as depicted in Fig. 3c and e. Therefore, calibration between the mole fractions and the characteristic Raman peaks is achieved *via* linear fitting:

$$x_{\mathrm{1octene}} = 0.53A_{1640}/A_{1450} \tag{1}$$

$$x_{\mathrm{cyC8}} = 0.42A_{700}/A_{1450} \tag{2}$$

Eqn (1) and (2) can be used for the quantitative measurement of hydrocarbon concentrations in microcells during interdiffusion experiments.

2.5 Experimental procedures

The experiments are divided into three series, as shown in Table 1. Series A and B are designed to investigate diffusion kinetics in channels with different depths, and the

Table 1 Series of experiments on interdiffusion in nanochannels

Series	Component #1	Component #2	Variables
A	1-Octene	*n*-Octane	Channel depth: 21, 37, 52, 85, 115, 173 nm
B	Cyclooctane	*n*-Octane	
C	1-Octene	*n*-Octane	Temperature: 295, 322, 345, 363, 383 K

interdiffusion components are *n*-octane and 1-octene, *n*-octane and cyclooctane, respectively. Series C is designed to investigate diffusion kinetics at different temperatures below the boiling points, and the interdiffusion components are *n*-octane and 1-octene.

Prior to the experiments, all chips are prepared as follows: (1) they are sequentially immersed in acetone, isopropanol, and deionized water for 12 hours each to remove impurities from the channels. (2) They undergo 15 minutes of plasma oxygen treatment to ensure strong wettability of the channel surfaces.

The experimental procedures are described below: (1) install the chips with the holder and the temperature control module (if heating is required), and connect the pipelines. Set the temperature of the PID controller, and wait until the temperature of the chip stabilizes. (2) Then, connect the pipelines to the vacuum pump. After the interior space of the chip is vacuumed, component #1 in the container is spontaneously injected and fill the interior space of the chip. (3) After that, the chip is placed on the microscope, and the laser forms a focused spot of about 3 μm in diameter at the position of the microcells to excite real-time Raman spectra collected by the spectrometer. The exposure time and the interval of each frame of spectra is 10 s and 20 s, respectively. (4) Next, connect the pipelines to the plunger pump. Component #2 in the pump is continuously injected into the microchannels and the interdiffusion in the nanochannels begins due to the concentration gradient between the microchannel and microcells. (5) When the collected Raman spectra no longer change over time, the diffusion experiment is completed.

After the experiments, the used chips are cleaned and then stored in a vacuum environment for reuse. The raw spectral data are processed in MATLAB software. The baseline signals are subtracted using the airPLS algorithm.[46] The concentration of component #1 in the microcells can be characterized by eqn (1) and (2), and then the relationship between the concentration and diffusion time can be obtained. The results of different nanochannels on the same chip are averaged.

2.6 Classical theory of diffusion

An illustration of the theoretical interdiffusion process in a nanochannel is shown in Fig. 4. It can be simplified as a one-dimensional diffusion problem because the concentration gradient is only along the length of the nanochannel. Let the length, width, and height (m) of the nanochannel be L, W, and H, and the volume (m^3) of the microcell be V. The characteristic diffusion time τ (s) of the nanochannel and microcell can be estimated as:

$$\tau = a^2/D \tag{3}$$

where D is the diffusion coefficient (m^2 s^{-1}), a is the characteristic length (m), $a = L$ for the nanochannel and a = 10 μm for the microcell. $L \gg 10$ μm, so the characteristic diffusion time of the nanochannel is much longer than that of the microcell, and the fluid concentration in the microcell can be regarded as uniformly distributed. In addition, since component #2 is continuously injected into the microchannel, the concentration of component #1 in the microchannel is always zero. A coordinate system is established with the length direction of the nanochannel as the x-axis, where $x = 0$ and $x = L$ represent two ends of the nanochannel. Let t be the diffusion time (s), and the mole concentrations (mol m^{-3}) of component #1 in the nanochannel and microcell be $C(x, t)$ and $C_0(t)$, respectively. According to Fick's diffusion law, the following differential equations can be listed:

$$\frac{\partial C}{\partial t} = D\frac{\partial^2 C}{\partial x^2} \tag{4}$$

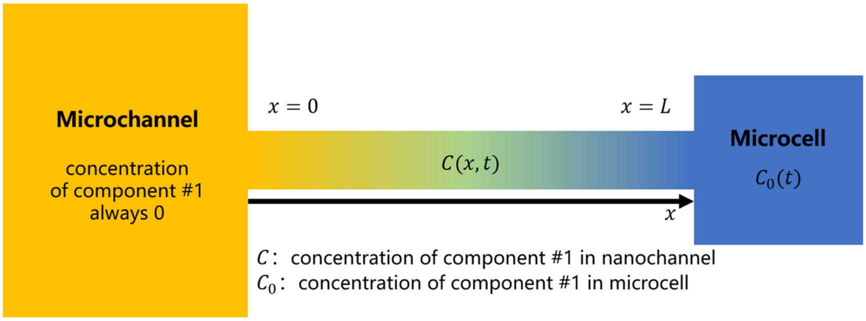

Fig. 4 Illustration of the theoretical interdiffusion process in a nanochannel.

$$V\frac{\mathrm{d}C_0}{\mathrm{d}t} = WHD\frac{\partial C}{\partial x}|_{x=L} \tag{5}$$

$$C|_{x=0} = 0,\ C|_{x=L} = \mathrm{C}_0 \tag{6}$$

The initial condition of $C(x, t)$ has no significant impact on the solution of $C(x, t)$ and $C_0(t)$ because the characteristic diffusion time of the nanochannel is estimated on the order of 0.1–10 s, while the whole experimental interdiffusion processes last for 10^3–10^4 s. Therefore, the dimensionless diffusion time Fo satisfies:

$$\mathrm{Fo} = t/\tau \gg 1 \tag{7}$$

which means that the interdiffusion in the nanochannel will be independent of the initial conditions quickly. To simplify the derivation of equations, assume the initial conditions to be:

$$C|_{t=0} = \frac{x}{L}C_0|_{t=0} \tag{8}$$

Generally, in a binary mixture with any concentration ratio, the interdiffusion coefficient D of component #1 can be expressed by Darken's equation:

$$D = (x_2D_1^* + x_1D_2^*)\cdot\left(1 + \frac{\partial \ln \gamma_1}{\partial \ln x_1}\right) \tag{9}$$

where x_1 and x_2 represent the mole fractions of component #1 and #2, D_1^* and D_2^* represent the self-diffusion coefficients ($\mathrm{m}^2\ \mathrm{s}^{-1}$) of component #1 and #2, and γ_1 is the activity coefficient of component #1.

For the interdiffusion of *n*-octane and cyclooctane, their molecular structures and self-diffusion coefficients are different, and the binary mixture cannot be treated as an ideal solution. Therefore, eqn (9) cannot be further simplified. However, for the interdiffusion of *n*-octane and 1-octene, their self-diffusion coefficients are approximately equal, and the binary mixture can be treated as ideal solution due to similar molecular structures and physical properties. Hence, $D_1^* = D_2^*$ and $\gamma_1 = 1$ are approximately satisfied and eqn (9) can be simplified to:

$$D = D_1^* = D_2^* \tag{10}$$

which means the interdiffusion coefficient is a constant independent of the fluid concentration. According to eqn (4)–(6) and (10), the analytical solutions of $C(x, t)$ and $C_0(t)$ can be obtained:

$$C = A\frac{x}{L}\exp\left(-\frac{WHD}{VL}t\right) \tag{11}$$

$$C_0 = A\exp\left(-\frac{WHD}{VL}t\right) \tag{12}$$

$$A = C_0|_{t=0} = \frac{\rho}{M_\mathrm{w}} \tag{13}$$

where A is a pre-exponential factor, ρ is the mass density (kg m^{-3}) and M_W is the molar mass of 1-octene (kg mol^{-1}). It can be observed that, if Fick's law is applicable, the concentration of 1-octene in the microcell will decrease exponentially with time, and the concentration in the nanochannel will vary linearly with distance. Diffusion coefficients D can therefore be calculated by fitting experimental results with eqn (12), which is the principle of our Concentraion Decay Method. In the following experiment, it will be examined whether the hydrocarbon diffusion in nanochannels conforms to the classical theory.

3. Results and discussion

3.1 Diffusion kinetics in nanochannels with different depths

Fig. 5a and b show the Raman spectra in a microcell at different diffusion times in a 37 nm-deep and 1000 μm-long channel in series A and B. In series A, both the 1640 cm^{-1} and 1450 cm^{-1} peaks are clearly observed at the initial moment, indicating that the borosilicate glass penetrated by the laser does not interfere with these peaks, and the Raman signal-to-noise ratio of the fluid in the microcell is acceptable. The 1450 cm^{-1} peak can be divided into two sub-peaks at about 1445 and 1460 cm^{-1}, which are related to the bending vibration of CH_2 and CH_3 groups, respectively.[47] As the interdiffusion continues, x_1octene in the microcell decreases, leading to a reduction in A_{1640}, while A_{1450} remains basically stable. After 3 hours, the 1640 cm^{-1} peak almost completely disappears, indicating that all 1-octene in the microcell has diffused into the microchannel, and the interdiffusion in nanochannels has completed. In series B, the phenomena are similar. The 700 cm^{-1} peak spends about 3 h to completely disappear, while the 1450 cm^{-1} peak remains basically unchanged.

It should be noted that the Raman spectrometer in our experiments collects the Raman scattering signals in a laser-focused sphere with a diameter of approximately 3 μm. This sphere is completely encapsulated by the microcell, so the collected Raman spectra can characterize the fluid components in the microcell. Based on eqn (1) and (2), the variation of x_1octene and x_cyC8 in the microcell over time is obtained, as shown in Fig. 5c and d. In series A, as the interdiffusion continues, x_1octene gradually decreases to zero. If the interdiffusion in the nanochannel conforms to Fick's law, x_1octene should exponentially decay over time. The experimental results show that x_1octene and time can be reasonably fitted by an exponential function with the fit goodness $R^2 > 0.95$, verifying the applicability of Fick's law. Although due to the environmental noise, there are inevitable random errors in A_{1640} and A_{1450} resulting in fluctuations of the obtained x_1octene around the fitted exponential curve, the overall trend of x_1octene over time is still regular. In series B, interestingly, x_cyC8 and time can also be reasonably fitted by an exponential function, although it is improper to simplify Darken's equation because of different physical properties of *n*-octane and cyclooctane. Therefore, in both series A and B,

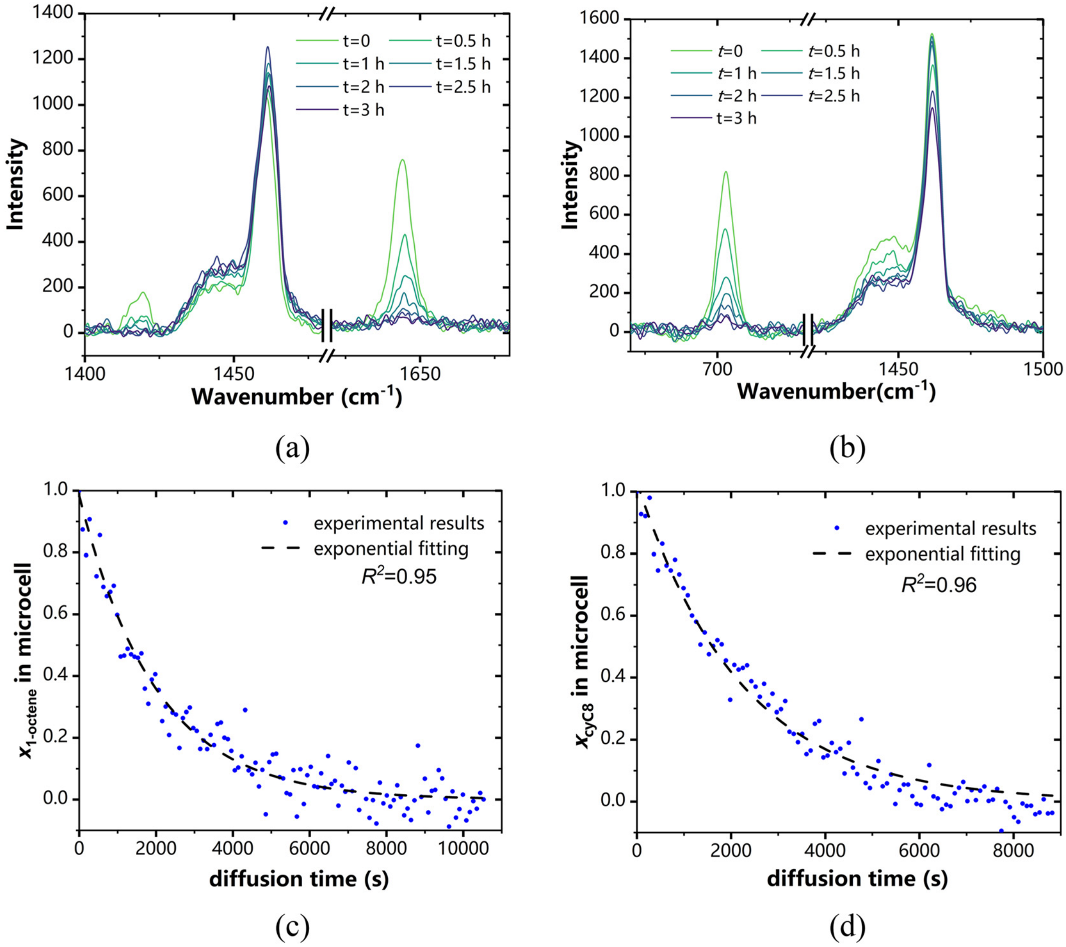

Fig. 5 Raman spectra and mole fractions in microcells during the interdiffusion process in a 37 nm-deep and 1000 μm-long nanochannel. (a) and (b) The change of the 1640 cm^{-1} peak with diffusion time in series A, and the change of the 700 cm^{-1} peak with diffusion time in series B. (c) and (d) $x_{1\text{octene}}$ in series A and x_{cyC8} in series B decaying exponentially over diffusion time.

apparent diffusion coefficients D in nanochannels can be measured based on Fig. 5c and d and eqn (12).

By the Concentration Decay Method, the diffusion coefficients in nanochannels with different depths are obtained, as shown in Fig. 6a and b. In series A, the bulk diffusion coefficient $D_{\text{bulk}} = 2.2 \times 10^{-9}$ m^2 s^{-1} is marked with a blue dotted line. Interestingly, we observe that all the measured D in channels with six different depths fluctuate around D_{bulk}, showing no obvious correlation with the channel depth. The maximum and minimum values of D are (2.76 ± 0.30) and (1.77 ± 0.21) × 10^{-9} m^2 s^{-1}, deviating by +25% and −20% from D_{bulk}, respectively. Due to potential subtle variations in the geometries and surface properties of different nanochannels at the same depth, it is reasonable to find that the measured D for different nanochannels may fluctuate. For example, for three nanochannels with a depth of 52 nm and a length of 300 μm, the measured D values are (2.44 ± 0.18), (2.56 ± 0.18), and (2.76 ± 0.30) × 10^{-9} m^2 s^{-1}, respectively. Additionally, we confirm that the measured D values in nanochannels with lengths of 1000 and 300 μm do not exhibit significant differences.

In series B, the bulk diffusion coefficients of *n*-octane and cyclooctane are marked with two blue dotted lines, and the interdiffusion coefficients are expected to lay between the two lines according to Darken's equation. The measured D values in channels with six different depths all lay between the two lines as expected, and show no obvious correlation with the channel depth and length as well. Based on the results of series A and B, we conclude that the diffusion kinetics in nanochannels with different depths and lengths exhibits no obvious deviation from the macroscopic scale, which also verifies the accuracy and reliability of our measurement of diffusion coefficients.

3.2 Diffusion kinetics in nanochannels at different temperatures

Next, in series C, interdiffusion of *n*-octane and 1-octene in channels with a depth of 37 nm at different temperatures is investigated. Five temperature points (295–383 K) are selected in the range below the boiling points. Since Raman scattering signals correlate with temperature,[48] it is necessary to

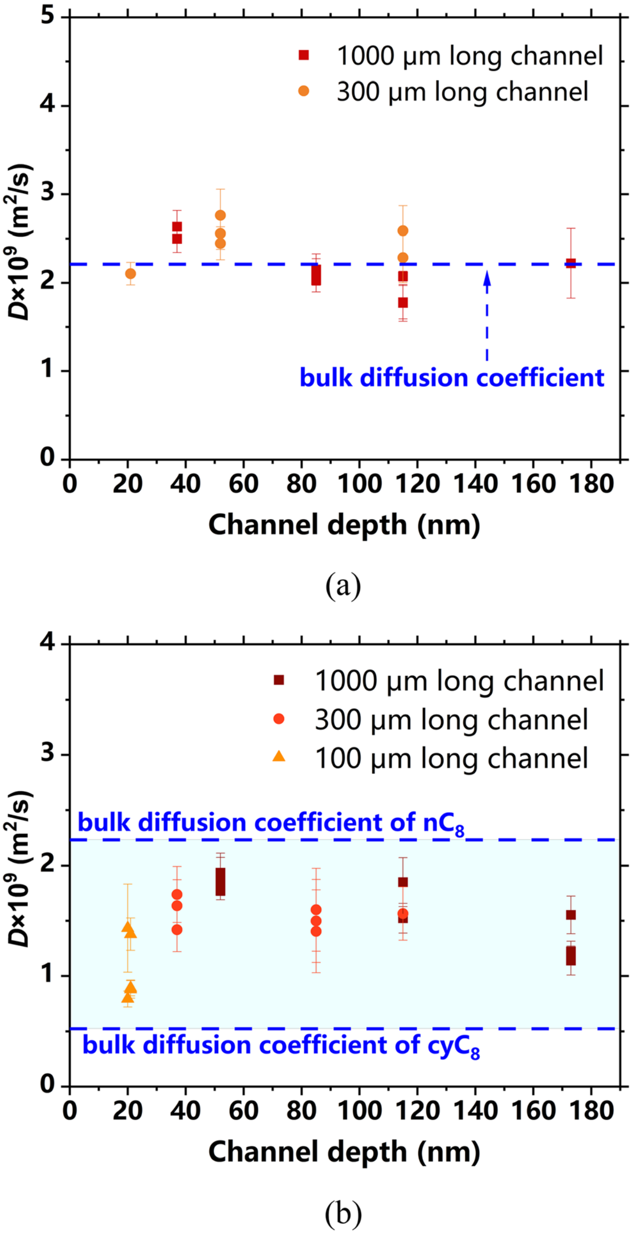

(a)

(b)

Fig. 6 Measured diffusion coefficients of (a) *n*-octane and 1-octene, and (b) *n*-octane and cyclooctane in nanochannels with different depths. The bulk diffusion coefficients D_{bulk} are indicated by blue dotted lines.

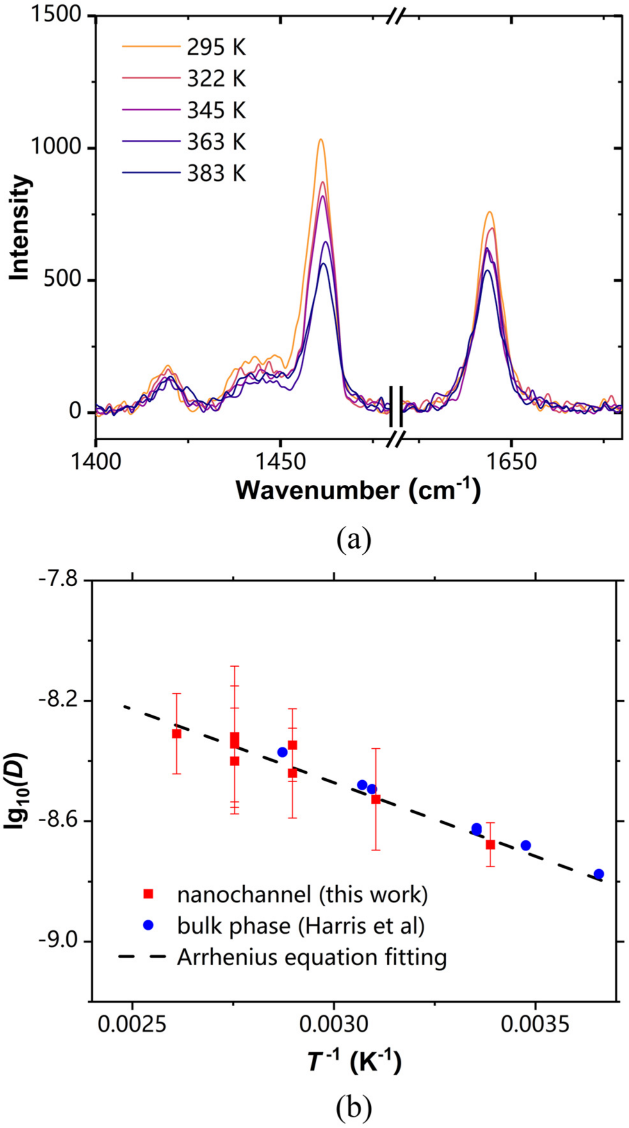

(a)

(b)

Fig. 7 Measurement of diffusion coefficients at different temperatures. (a) 1450 and 1640 cm^{-1} Raman peaks of 1-octene in a microcell at different temperatures. (b) Diffusion coefficients of *n*-octane and 1-octene in nanochannels at different temperatures as obtained from the experiments. Blue data points represent diffusion coefficients in the bulk phase.[49]

examine whether temperature will affect the accuracy of D measurement by Raman spectroscopy. Taking pure 1-octene as an example, the temperature dependence of Raman spectra of fluid in a microcell is shown in Fig. 7a. As the temperature increases, the wavenumber positions of 1450 and 1640 cm^{-1} peaks slightly shift, and the full width at half maxima (FWHM) remain almost unchanged, while the peak intensities and areas obviously decrease. Although the peak areas are temperature-dependent, eqn (1) and (2) can still be used for fluid concentration calibration at different temperatures provided that the proportion coefficients are adjusted. Furthermore, the mole fraction of 1-octene in the microcell is found to still exhibit exponential decay with diffusion time at different temperatures.

By the Concentration Decay Method, the diffusion coefficients D in nanochannels at different temperatures are obtained, as shown in Fig. 7b. The red data points in the figure represent the measured D in the 37 nm-deep channel in our experiments, while the blue data points represent D in the bulk phase measured by Harris *et al.*[49] As the temperature increases, the measured D values in the nanochannel gradually increase from (2.10 ± 0.15) × 10^{-9} m^2 s^{-1} at 295 K to (4.9 ± 0.6) × 10^{-9} m^2 s^{-1} at 383 K, showing the same trend as D in the bulk phase. Considering the experimental uncertainty, the measured D values in the nanochannel at different temperatures exhibit no obvious deviation from those in the bulk phase.

The increase in fluid temperature leads to intensified molecular motion, which increases the diffusion kinetics. By applying the Eyring rate theory, it can be deduced that the relationship between D and thermodynamic temperature T conforms to the expression of Arrhenius equation:[50]

$$D = D_0 \exp\left(-\frac{E_a}{RT}\right) \tag{14}$$

where D_0 is a pre-exponential factor, E_a is the diffusion activation energy, and R is the ideal gas constant. The $\lg_{10}(D) - T^{-1}$ relationship is fitted using eqn (14) and the fitting curve is marked with the black dashed line in Fig. 7b. The diffusion kinetics in nanochannels also conforms to the Eyring rate theory, and the measured D at different temperatures can be predicted by the Arrhenius equation. In conclusion, the diffusion kinetics in nanochannels at different temperatures exhibits no obvious deviation from the macroscopic scale as well.

3.3 Influencing factors of measurement

Factors that potentially influence the measurement results of D are discussed below.

(1) **Fluid–wall interactions.** The intention of this study is to explore the extent to which fluid–wall interactions affects the diffusion kinetics in nanochannels. Core-scale experiments failed to decouple whether slower diffusion kinetics results from longer diffusion paths or slower molecular diffusion affected by fluid–wall interactions;[17] meanwhile in our experiments, the "channel-channel-cell" structure can reflect molecular diffusion driven by concentration gradients without the influence of tortuosity. We discover that for *n*-octane, 1-octene and cyclooctane, fluid–wall interactions have no significant effect on the molecular diffusion kinetics in channels with a minimum depth of 21 nm. Previous molecular simulations indicated that the nanoconfinement effect of hydrocarbons in nanochannels leads to a reduction in the component of D normal to the channel surface, while the component tangential to the surface remains almost unchanged.[23] In our experiments, the concentration gradient is along the length of nanochannels; thus, the measured D values reflect diffusion kinetics in the direction normal to the wall which is less sensitive to fluid–wall interactions. If the channel depth or pore diameter is further reduced, it has been revealed that long-chain hydrocarbons will diffuse faster in carbon nanotubes with an inner diameter of about 1 nm, or diffuse slower in kerogen organic pores with diameters ranging from 0.1 to 1.5 nm.[15,51] It is reasonable to infer that for hydrocarbons, the threshold pore size at which fluid–wall interactions become the dominant mechanism for diffusion may be between 2 and 20 nm.

Some other experiments have reported anomalous diffusion behaviour of macromolecules in channels with similar depths,[31–33] suggesting a more rigorous discussion on the relative ratio of the characteristic size of diffusing molecules L_{mol} to the channel depth H. In our experiments, the length of a *n*-octane or 1-octene molecule is about 1.1 nm, the diameter of a cyclooctane molecule is about 0.6 nm, and $L_{\mathrm{mol}}/H < 0.05$. If the size of diffusing molecules increases, L_{mol}/H will increase, and the effect of fluid–wall interactions on diffusion will be more significant. For example, Zhong *et al.*[33] reported that the apparent diffusion coefficient of Rhodamine B decreases by two orders of magnitude when $L_{\mathrm{mol}}/H \approx 0.2$, and Yang *et al.*[32] reported that the diffusion of proteins should be explained by a single-file regime when $L_{\mathrm{mol}}/H \approx 0.5$. In addition, whether long-range electrostatic forces exist should also be considered. In our experiments, the hydrocarbons are non-polar and non-electrolyte fluids, indicating that the near-wall fluid is mainly subject to van der Waals forces and electrostatic forces can be neglected. In the presence of electrostatic forces, diffusion is expected to be more complicated. For example, Schoch *et al.*[52] reported that the pH value of solution can regulate the diffusion coefficient of surface-charged proteins in nanochannels ($L_{\mathrm{mol}}/H \approx 0.2$) due to the Donnan effect.

(2) **Temperature increase due to laser irradiation.** The high-energy laser focused on fluid may cause a temperature increase, and its impact on the measured D should be examined. Let the increase in the average temperature of fluid in microcells during Raman sampling be ΔT. Because the silicon substrate and glass cover are significantly larger than the microcells and the thermal conductivity of silicon and glass is much greater than that of hydrocarbons, the temperature at the microcell surfaces can be approximated as the room temperature. Besides, the heat dissipation through the nanochannels is negligible. Therefore, according to the law of energy conservation, we have:

$$P_{\mathrm{ad}} \cdot t_1 = h \cdot T\Delta \cdot 6b^2 \cdot t_2 \tag{15}$$

$$P_{\mathrm{ad}} = P_{\mathrm{laser}} \alpha b \tag{16}$$

$$\mathrm{Nu} = hb/k_1 \tag{17}$$

where P_{laser} and P_{ad} are the laser power and the liquid absorption power, t_1 and t_2 are the exposure time and sampling interval of Raman spectra, h is the convective heat transfer coefficient between the liquid in microcells and the microcell surfaces, b is the side length of microcells, α is the absorption coefficient of the liquid at a wavelength of 532 nm, k_1 is the thermal conductivity of the liquid, Nu is the Nusselt number. Natural convection heat transfer in microcells is suppressed (Rayleigh number < 1); thus, thermal conduction is the dominant heat transfer mechanism, and Nu is approximately equal to unity. Setting P_{laser} = 100 mW, t_1 = 10 s, t_2 = 30 s, b = 10 μm, α = 0.1 cm^{-1}, and k_1 = 0.127 W (m K^{-1}), and substituting them into eqn (15)–(17), we estimate that ΔT = 0.44 K. Assuming the relationship between D and T obeys the Arrhenius equation, then ΔT would cause D to increase by about 0.02×10^9 m^2 s^{-1}, which is negligible compared to the experimental uncertainty.

(3) Air dissolved in the fluid. Since the interior space of nanofluidic chips cannot achieve absolute vacuum, after 1-octene is spontaneously aspirated, air bubbles may exist in some microcells. As the air dissolves into the oil phase, the bubbles gradually decrease in size until they disappear. The dissolved air would reduce the oil viscosity, and D is inversely proportional to the viscosity according to the Stokes–Einstein equation; therefore, it would cause the measured D to be larger than the actual value. However, the saturated mole fraction of dissolved N_2 and O_2 in hydrocarbons at 295 K and atmospheric pressure is around 1×10^{-3}, which has limited impact on D.[53] Besides, the effect of dissolved air on interdiffusion is independent of the channel depth, so it does not invalidate the conclusion that the measured D is independent of the channel depth.

(4) Species-driven advection. Although there is no pressure-driven advection in nanochannels, the existence of species-driven advection, such as diffusioosmotic, diffusiophoresis[54,55] and solutal Marangoni effects,[56] should be discussed. The main mechanism of diffusioosmotic is the distorted structure of the electrical double layer (EDL) due to a gradient in electrolyte solutes, while diffusiophoresis is the motion of a mobile particle in electrolyte solutions driven by diffusioosmotic flow.[54] In our experiments, the mixtures of *n*-octane, 1-octene and cyclooctane are non-electrolyte, and there is no suspended colloidal particle, so these EDL-induced effects can be ignored. The solutal Marangoni effect happens when there is a surface tension gradient due to concentration differences. In our experiments, the single-phase and multi-component hydrocarbons fill the nanochannels, and the concentration gradient can cause a gradient in the solid–liquid interfacial tension. If neglecting the influence of the solid wall, we estimate that the Marangoni number $\mathrm{Ma} = \Delta\sigma H/\mu D$ in nanochannels is on the order of 1. However, the hydrocarbon molecules near the interface are affected by the solid wall with strong wettability and the no-slip boundary condition is applicable, which significantly suppresses the generation of Marangoni flow. In conclusion, we believe species-driven advection in nanochannels can be ignored in our experiments, indicating the rationality of the use of a purely diffusive model as mentioned in section 2.6.

3.4 Advantages of the method

Our study proposes the Concentration Decay Method to investigate fluid diffusion kinetics in nanoconfined space by combining nanofluidic chips and micro-Raman spectroscopy. It has mainly three advantages: (1) Compared to traditional experiments, this method can decouple the influence of pore structure and fluid–wall interactions on diffusion coefficients by designing the space where interdiffusion occurs. (2) Compared to molecular simulations, this method fills the gap of diffusion in nanopores with diameters ranging from 10 to 100 nm. Moreover, with the development of nanofluidic technology, investigation on diffusion in shallower and more complex channels will become possible. (3) Compared to nanofluidic experiments *via* conventional optical methods, this method can be applicable to more types of diffusing components as long as there are significant differences in the Raman characteristic peaks.

In further studies, fluid diffusion kinetics in nanochannels with more types of components, more complex channel structures and smaller depth of the channel can be systematically investigated by this method. This will provide more insight into fluid transport in nanopores and facilitate energy conversion and utilization.

4. Conclusions

In this work, a novel Concentration Decay Method combining nanofluidics and micro-Raman spectroscopy to investigate fluid diffusion in nanochannels is proposed. A "channel-channel-cell" structure in nanofluidic chips is specifically designed for detecting diffusion kinetics in nanochannels. By this method, an experimental investigation on interdiffusion of the *n*-octane–1-octene mixture and *n*-octane–cyclooctane mixture in channels with a minimum depth of 21 nm at different temperatures (295–383 K) is conducted, and diffusion coefficients are obtained.

The conclusions are as follows: (1) the interdiffusion in nanochannels still conforms to Fick's diffusion law, and the measured diffusion coefficients in nanochannels with a minimum depth of 21 nm exhibit no obvious deviation from the bulk phase. (2) The measured diffusion coefficients in nanochannels at different temperatures still exhibit no obvious deviation from the bulk phase and can be predicted by the Arrhenius equation. (3) The proposed novel method decouples the influence of pore structure and fluid–wall interactions on diffusion kinetics, fills the gap of research on diffusion in pores with diameters ranging from 10 to 100 nm, and is applicable to more types of fluids. Our work deepens the understanding of multi-component fluid transport in nanopores.

Conflicts of interest

The work described has not been published previously and it is not under consideration for publication elsewhere. The authors declare that they have no known competing financial interests or personal relationships that could have appeared to influence the work reported in this paper.

Data availability

The authors confirm that the data supporting the findings of this study are available within the article.

Acknowledgements

This work was supported by the National Natural Science Foundation of China (No. U22B6004 and No. U22B20145).

References

1 D. J. Soeder, *Fuel*, 2018, **163**, 399–420.
2 X. Wang, G. Zhang, W. Tang, D. Wang, K. Wang, J. Liu and D. Du, *Energy Geosci.*, 2022, **3**, 282–289.
3 X. Wang, J. Li, W. Jiang, H. Zhang, Y. Feng and Z. Yang, *Adv. Geo-Energy Res.*, 2022, **6**(6), 454–459.
4 T. Hu, F. Jiang, X. Pang, Y. Liu, G. Wu, K. Zhou, H. Xiao, Z. Jiang, M. Li, S. Jiang, L. Huang, D. Chen and Q. Meng, *Pet. Explor. Dev.*, 2024, **51**(1), 127–140.
5 Z. Kang, Y. Zhao and D. Yang, *Appl. Energy*, 2020, **269**, 115121.
6 F. Tuero, M. Crotti and I. Labayen, *SPE Latin America and Caribbean Petroleum, Engineering Conference*, 2017, p. SPE-185560-MS.
7 L. Wang, Y. Zhang, R. Zou, R. Zou, L. Huang, Y. Liu, Z. Meng, Z. Wang and H. Lei, *Int. J. Hydrogen Energy*, 2023, **48**, 37134–37165.
8 A. Suleimenova, K. D. Bake, A. Ozkan, J. J. Valenza, R. L. Kleinberg, A. K. Burnham, N. Ferralis and A. E. Pomerantz, *Fuel*, 2014, **135**, 492–497.
9 J. Li, H. Li, W. Jiang, M. Cai, J. He, Q. Wang and D. Li, *Sci. Rep.*, 2024, **14**, 16896.
10 Y. Qu, S. Ouyang, J. Gao, J. Shi, Y. Wu, Y. Cheng, Z. Zhou, Z. Lyu, W. Sun and H. Wu, *Fractal Fract.*, 2024, **8**, 588.
11 K. L. McCormack, J. Li, T. J. Yoklavich and Y. Xia, *Phys. Fluids*, 2024, **36**(09), 1301.
12 J. Kärger and D. M. Ruthven, *New J. Chem.*, 2016, **40**, 4027.
13 J. Kärger, D. M. Ruthven and R. Valiullin, *Adsorption*, 2021, **27**, 267–281.
14 K. Zeng, P. Jiang and R. Xu, *Int. J. Heat Mass Transfer*, 2023, **210**, 124178.
15 J. Yuan, M. Gao, Z. Liu, X. Tang, Y. Tian, G. Ma, M. Ye and A. Zheng, *Nat. Commun.*, 2023, **14**, 1735.
16 W. Yuan, Z. Pan, X. Li, Y. Yang, C. Zhao, L. D. Connell, S. Li and J. He, *Fuel*, 2014, **117**, 509–519.
17 Z. Wanyan, Y. Liu, Z. Li, C. Zhang, Y. Liu and T. Xue, *Adv. Geo-Energy Res.*, 2023, **7**(1), 39–48.
18 S. Wang, F. Javadpour and Q. Feng, *Fuel*, 2016, **171**, 74–86.
19 H. Sui, F. Zhang, Z. Wang, D. Wang and Y. Wang, *J. Mol. Liq.*, 2020, **305**, 112745.
20 Q. Rao, Y. Xia, J. Li, M. Deo and Z. Li, *J. Mol. Liq.*, 2021, **344**, 117673.
21 P. Asai, P. Panja, R. Velasco and M. Deo, *Sci. Rep.*, 2021, **11**, 11015.
22 W. Zhang, Q. Feng, S. Wang and X. Xing, *J. Mol. Liq.*, 2019, **290**, 111183.
23 L. Zheng, Q. Zhao, M. J. Adams, A. Alexiadis, Y. Wang, H. Jin and L. Guo, *J. Mol. Liq.*, 2024, **414**, 126110.
24 M. A. Alibakhshi, Q. Xie, Y. Li and C. Duan, *Sci. Rep.*, 2016, **6**, 24936.
25 H. Li, J. Zhong, Y. Pang, S. H. Zandavi, A. H. Persad, Y. Xu, F. Mostowfi and D. Sinton, *Nanoscale*, 2017, **9**, 9556–9561.
26 S. Mozaffari, P. Tchoukov, A. Mozaffari, J. Atias, J. Czarnecki and N. Nazemifard, *Colloids Surf., A*, 2017, **513**, 178–187.
27 H. Lu, Y. Xu, C. Duan, P. Jiang and R. Xu, *Energy Fuels*, 2022, **36**, 5267–5275.
28 B. Bao, S. H. Zandavi, H. Li, J. Zhong, A. Jatukaran, F. Mostowfi and D. Sinton, *Phys. Chem. Chem. Phys.*, 2017, **19**, 8223.
29 J. Zhong, Y. Zhao, C. Lu, Y. Xu, Z. Jin, F. Mostowfi and D. Sinton, *Langmuir*, 2018, **34**, 9927–9935.
30 X. Cheng, M. D. Ooms and D. Sinton, *Lab Chip*, 2016, **16**, 256–260.
31 A. Balducci, P. Mao, J. Han and P. S. Doyle, *Macromolecules*, 2006, **39**(18), 6273–6281.
32 S. Y. Yang, J. A. Yang, E. S. Kim, G. Jeon, E. J. Oh, K. Y. Choi, S. K. Hahn and J. K. Kim, *ACS Nano*, 2010, **4**(7), 3817–3822.
33 J. Zhong, S. Talebi, Y. Xu, Y. Pang, F. Mostowfi and D. Sinton, *Lab Chip*, 2018, **18**(4), 568–573.
34 S. G. da Costa, A. Richter, U. Schmidt, S. Breuninger and O. Hollricher, *Morphologie*, 2019, **103**, 11–16.
35 J. Toporski, T. Dieing and O. Hollricher, *Confocal Raman Microscopy*, Springer Series in Surface Sciences, Springer International Publishing AG, 2018.
36 T. H. Kauffmann and M. D. Fontana, *Sens. Actuators, B*, 2005, **209**, 154–161.
37 R. Gieleciak, A. Hall, K. Michaelian and J. Chen, *Energy Fuels*, 2023, **37**, 13698–13709.
38 J. B. Salmon, A. Ajdari and P. Tabeling, *Appl. Phys. Lett.*, 2005, **86**, 094106.
39 N. Liu, C. Aymonier, C. Lecoutre, Y. Garrabos and S. Marre, *Chem. Phys. Lett.*, 2012, **551**, 139–143.
40 C. Peters, L. Wolff, S. Haase, J. Thien, T. Brands, H. J. Koss and A. Bardow, *Lab Chip*, 2017, **17**, 2768.
41 Q. Xie, F. Xin, H. G. Park and C. Duan, *Nanoscale*, 2016, **8**(47), 19527–19535.
42 Q. Xie, M. A. Alibakhshi, S. Jiao, Z. Xu, M. Hempel, J. Kong, H. G. Park and C. Duan, *Nat. Nanotechnol.*, 2018, **13**(3), 238–245.
43 F. F. Cleveland, *J. Chem. Phys.*, 1943, **11**, 1–6.
44 Y. V. Shemouratov, K. A. Prokhorov, Y. G. Nikolaeva, P. P. Pashinin, A. A. Kovalchuk, A. N. Klyamkina, P. M. Nedorezova, K. V. Demidenok, Y. A. Lebedev and E. M. Antipov, *Laser Phys.*, 2008, **18**, 554–567.
45 P. S. Tofts, D. Lloyd, C. A. Clark, G. J. Barker, G. J. Parker, P. McConville, C. Baldock and J. M. Pope, *Magn. Reson. Med.*, 2000, **43**, 368–374.
46 Z. Zhang, S. Chen, Y. Liang, Z. Liu, Q. Zhang, L. Ding, F. Ye and H. Zhou, *J. Raman Spectrosc.*, 2010, **41**, 659–669.
47 Y. V. Shemouratov, K. A. Prokhorov, Y. G. Nikolaeva, P. P. Pashinin, A. A. Kovalchuk, A. N. Klyamkina, P. M. Nedorezova, K. V. Demidenok, Y. A. Lebedev and E. M. Antipov, *Laser Phys.*, 2008, **18**, 554–567.
48 M. R. Abel, T. L. Wright, W. P. King and S. Graham, *IEEE Trans. Compon., Packag. Technol.*, 2007, **30**(2), 200–208.

49 K. R. Harris, J. J. Alexander, T. Goscinska, R. Malhotra, L. A. Woolf and J. H. Dymond, *Mol. Phys.*, 1993, **78**(1), 235–248.

50 M. Mantina, L. Q. Chen and Z. K. Liu, *Defect Diffus. Forum*, 2009, **294**, 1–13.

51 K. Falk, B. Coasne, R. Pellenq, F. J. Ulm and L. Bocquet, *Nat. Commun.*, 2015, **6**, 6949.

52 R. B. Schoch, A. Bertsch and P. Renaud, *Nano Lett.*, 2006, **6**(3), 543–547.

53 L. N. Mizerovsky and K. P. Smirnova, *Russ. Chem. Bull.*, 2010, **59**, 673–676.

54 S. Shim, *Chem. Rev.*, 2022, **122**, 6986–7009.

55 A. Ganguly, B. M. Alessio and A. Gupta, *Front. Sens.*, 2023, **4**, 1322906.

56 S. Park, L. Liu, C. Demirkir, O. Heijden, D. Lohse, D. Krug and M. T. M. Koper, *Nat. Chem.*, 2023, **15**, 1532–1540.